International Journal of Engineering Science 86 (2015) 44–59

Contents lists available at ScienceDirect

International Journal of Engineering Science

journal homepage: www.elsevier.com/locate/ijengsci

A method for characterisation of the static elastic properties of the porous frame of orthotropic open-cell foams

Christophe Van der Kelen *, Jacques Cuenca, Peter Göransson

KTH Royal Institute of Technology, Marcus Wallenberg Laboratory for Sound and Vibration Research, Teknikringen 8, SE-10044 Stockholm, Sweden

ARTICLE INFO

Article history:
Received 22 August 2013
Received in revised form 23 September 2014
Accepted 8 October 2014
Available online 9 November 2014

Keywords:
Porous materials
Open-cell foams
Inverse estimation
Anisotropy
Hooke's tensor

ABSTRACT

This paper proposes a method to identify the static, fully relaxed elastic Hooke's matrix of a porous open-cell material. The moduli are estimated through an inverse estimation method, by performing a fit of a numerical model on the measured displacements on the faces of the porous material. These displacements are obtained from a static compression along each of the three coordinate axes. The material is modelled as an orthotropic equivalent solid, of which the principal directions are not necessarily aligned with the orthonormal coordinate system in which the experiments are conducted. The angles of relative orientation accounting for the misalignment are among the properties to be estimated. The focus in this paper is on the methodology itself, and its validity is verified by applying the method to four artificial materials with different levels of anisotropy. In addition, the robustness of the method to perturbations on the input data is investigated.

1. Introduction

The properties of lightweight open-cell porous materials for acoustic applications are highly dependent on the production process. The production process itself influences the micro-structure and geometry of the material, possibly inducing anisotropy in the macroscopic properties of the material. At present, the degree of anisotropy in the porous material due to the production process is unclear, and the implications of the anisotropy are not yet fully understood.

The influence of anisotropy in porous materials on the predicted acoustic performance of multi-layered arrangements has been studied and reported as significant by Göransson and Hörlin (2010), Hörlin and Göransson (2010) and Lind Nordgren, Göransson, Deü, and Dazel (2013). In order to confirm the results and to assess these effects in a real foam, the degree of anisotropy, together with the corresponding anisotropic properties of a material, needs to be determined.

Several authors have attempted the characterisation of the anisotropic properties of porous materials, often assuming that the material exhibits a certain symmetry, and that the principal material directions are aligned with the imposed coordinate axes. Jaouen, Renault, and Deverge (2008) give an overview of the available experimental methods for elastic and damping characterisation of acoustical porous materials. The studied methods are all under quasi-static or dynamic excitation of the material, and only the method described by Melon, Mariez, Ayrault, and Sahraoui (1998) allows for characterisation of transversely isotropic materials, assuming that the principal material directions are known.

In addition, most real porous materials are exhibiting an anelastic behaviour, since the predominant component of porous materials is usually an elastomer for which the rubbery regime often spans room temperature (Gibson & Ashby, 1997). A

---

* Corresponding author.
E-mail address: cjfvdk@kth.se (C. Van der Kelen).

http://dx.doi.org/10.1016/j.ijengsci.2014.10.005
0020-7225/

method for characterisation of the elastic and anelastic properties of open-cell foams was recently proposed by Cuenca and Göransson (2012) and applied to melamine foam by Cuenca, Van der Kelen, and Göransson (2014). The reported method uses the augmented Hooke's law (Dovstam, 2000), separating the stiffness matrix into a static, elastic matrix and a frequency-dependent, anelastic matrix. This separation was motivated by Biot (1954) who introduced the concept of hidden thermodynamic variables, and described the dynamic elastic moduli of the solid as a superposition of elastic and anelastic contributions. The focus of the current paper is on the full characterisation of the anisotropic static elastic properties of a porous material, which has not been attempted yet to the knowledge of the authors.

The present work is an important step towards the generalisation of the work of Cuenca and Göransson (2012) and Cuenca et al. (2014), where one of the assumptions made was that the elastic and anelastic moduli are collinear. The method proposed in this paper allows to remove this restriction, as it provides the fully relaxed, elastic properties independently, and the same material can be characterised using both methods, with the resulting static elastic matrix and the frequency-dependent anelastic matrices possibly having different degrees of anisotropy. The possibility of these matrices possessing different symmetries was already reported by Dovstam (2000) and Biot (1954). Whether or not this is the case for the elastomers that constitute the solid frame of porous foams, is an open question.

The main contribution of this paper is to propose a method for the characterisation of the anisotropic static elastic properties of a porous material. As a proof of concept concerning the feasibility of the inverse estimation approach proposed, numerically simulated measurements are used as targets in the inverse estimation. The current paper starts with the material model and the characterisation method, which is then applied to four fictitious materials, one isotropic, one transversely isotropic, one orthotropic and one anisotropic material sample, to verify the method and its applicability for the present purpose. A study of the numerical robustness of the method is included as well.

2. Material model

Biot (1956) described the constitutive laws for porous materials, which consist of a solid phase and a fluid phase, most frequently air in acoustic applications. In the case of open-cell porous materials, the fluid phase only takes part in the dynamic deformation (Melon et al., 1998). Therefore, the static structural properties of the material, such as elasticity, can conveniently be described in the absence of the fluid phase. Then, only the solid frame of the material is here considered and the Hooke's law for the material may be written as

$$\underline{\boldsymbol{\sigma}}(\omega) = \mathbf{H}(\omega)\underline{\boldsymbol{\varepsilon}}(\omega), \tag{1}$$

giving the relation between the frequency-dependent stresses and strains in the material in vacuum, where $\mathbf{H}(\omega)$ is the stiffness or Hooke's matrix. For the notation of the stresses and strains, the convention used is

$$\begin{aligned} \underline{\boldsymbol{\sigma}} &= [\,\sigma_{11} \quad \sigma_{22} \quad \sigma_{33} \quad \sigma_{23} \quad \sigma_{31} \quad \sigma_{12}\,]^{\mathrm{T}}, \\ \underline{\boldsymbol{\varepsilon}} &= [\,\varepsilon_{11} \quad \varepsilon_{22} \quad \varepsilon_{33} \quad 2\varepsilon_{23} \quad 2\varepsilon_{31} \quad 2\varepsilon_{12}\,]^{\mathrm{T}}. \end{aligned} \tag{2}$$

The stiffness matrix $\mathbf{H}(\omega)$ may be rewritten according to the augmented Hooke's law (Dovstam, 2000) as a superposition of an elastic, frequency-independent part describing the fully relaxed material deformation, and an anelastic, frequency-dependent part for the reversible visco-elastic deformation,

$$\mathbf{H}(\omega) = \mathbf{H}^{(0)} + \tilde{\mathbf{H}}(\omega). \tag{3}$$

This paper focuses on the characterisation of the static, frequency-independent part $\mathbf{H}^{(0)}$ of the Hooke's matrix. A proof of concept for estimation of the frequency-dependent part $\tilde{\mathbf{H}}(\omega)$ is given by Cuenca and Göransson (2012), and an application to a melamine foam in Cuenca et al. (2014), in which the material should be placed in vacuum conditions during the experiment to extract the influence of air. For the static part of the Hooke's matrix discussed here, the material needs not be in vacuum (Hörlin & Göransson, 2010), given that the deformation is slow enough. As no pressure variation is present in the material, it may be modelled as an equivalent solid material.

The anisotropic Hooke's matrix $\mathbf{H}_{\mathrm{a}}^{(0)}$ for an orthotropic material, presented in a coordinate system that is not necessarily aligned with the natural coordinate system is given as

$$\mathbf{H}_{\mathrm{a}}^{(0)} = \begin{bmatrix} H_{\mathrm{a},11}^{(0)} & H_{\mathrm{a},12}^{(0)} & H_{\mathrm{a},13}^{(0)} & H_{\mathrm{a},14}^{(0)} & H_{\mathrm{a},15}^{(0)} & H_{\mathrm{a},16}^{(0)} \\ & H_{\mathrm{a},22}^{(0)} & H_{\mathrm{a},23}^{(0)} & H_{\mathrm{a},24}^{(0)} & H_{\mathrm{a},25}^{(0)} & H_{\mathrm{a},26}^{(0)} \\ & & H_{\mathrm{a},33}^{(0)} & H_{\mathrm{a},34}^{(0)} & H_{\mathrm{a},35}^{(0)} & H_{\mathrm{a},36}^{(0)} \\ & & & H_{\mathrm{a},44}^{(0)} & H_{\mathrm{a},45}^{(0)} & H_{\mathrm{a},46}^{(0)} \\ & (\mathrm{sym}) & & & H_{\mathrm{a},55}^{(0)} & H_{\mathrm{a},56}^{(0)} \\ & & & & & H_{\mathrm{a},66}^{(0)} \end{bmatrix}. \tag{4}$$

The Hooke's matrix $\mathbf{H}_\mathrm{a}^{(0)}$ consists of 21 independent terms and can be rewritten as a transformation of the orthotropic Hooke's matrix $\mathbf{H}^{(0)}$, defined by nine entries in its natural coordinate system, by multiplication with a Bond matrix $\mathbf{A}_\varepsilon$ (Carcione, 2007; Slawinski, 2010), such that

$$\mathbf{H}_\mathrm{a}^{(0)} = \left(\mathbf{A}_\varepsilon^\mathrm{T}\right)^{-1} \mathbf{H}^{(0)} (\mathbf{A}_\varepsilon)^{-1}. \tag{5}$$

The matrix $\mathbf{A}_\varepsilon$ is given in Appendix A. The entries of $\mathbf{A}_\varepsilon$ are the elements of transformation matrix $\mathbf{a}$, defined by a successive rotation around the fixed $x,\ y$, and z axes of the natural coordinate system by angles $\alpha,\ \beta$ and γ respectively, as

$$\mathbf{a} = \mathbf{R}(x,\alpha)\ \mathbf{R}(y,\beta)\ \mathbf{R}(z,\gamma). \tag{6}$$

The rotation matrices $\mathbf{R}(x,\alpha),\ \mathbf{R}(y,\beta), \mathbf{R}(z,\gamma)$ may be found in Appendix A as well. Other sets of Euler angles are possible, and for each combination of rotations, a unique set of Euler angles exists, leading eventually to the same transformed matrix.

The stiffness matrix $\mathbf{H}^{(0)}$ can be rewritten in its natural coordinate system in terms of engineering constants as

$$\mathbf{H}^{(0)} = \begin{bmatrix} \frac{1}{E_1} & -\frac{\nu_{21}}{E_2} & -\frac{\nu_{31}}{E_3} & 0 & 0 & 0 \\ -\frac{\nu_{12}}{E_1} & \frac{1}{E_2} & -\frac{\nu_{32}}{E_3} & 0 & 0 & 0 \\ -\frac{\nu_{13}}{E_1} & -\frac{\nu_{23}}{E_2} & \frac{1}{E_3} & 0 & 0 & 0 \\ 0 & 0 & 0 & \frac{1}{G_{23}} & 0 & 0 \\ 0 & 0 & 0 & 0 & \frac{1}{G_{31}} & 0 \\ 0 & 0 & 0 & 0 & 0 & \frac{1}{G_{12}} \end{bmatrix}^{-1}, \tag{7}$$

where $E_1,\ E_2$ and E_3 are the Young's moduli in directions 1, 2 and 3 respectively, and ν_{ij} is the Poisson ratio for transverse strain in the j direction when loaded in the i direction. G_{ij} are the shear moduli in the (i,j) planes respectively (Jones, 1999).

3. Characterisation method

The approach for characterisation of the static orthotropic Hooke's matrix $\mathbf{H}_a^{(0)}$ of poroelastic materials uses a set of measured displacements $\mathbf{u}^\mathrm{EXP}$ as targets of an inverse estimation procedure. In the latter, the experimental setup is replicated in a finite element model, including the material model described above and providing the corresponding simulated displacements $\mathbf{u}^\mathrm{FE}$ for a set of elastic moduli. These are varied until the difference between measured and simulated displacements is minimised. Such minimisation procedure is performed numerically by means of an optimisation algorithm.

3.1. Experimental setup

The displacements $\mathbf{u}^\mathrm{EXP} = \{u, v, w\}$ are measured in an appropriate setup on a cubic material sample which is compressed by $d_\mathrm{a} = L_0 - L_1$, subsequently in all three coordinate directions, where subscript 0 refers to the state of the sample prior to compression and subscript 1 to the state thereafter. In addition to the measurement of the displacements, the force needed to compress the material sample by d_a must be measured for a complete characterisation of the Hooke's matrix.

In order to design a practical experiment, it was chosen to apply a compression to a cubic sample of porous material, and to simultaneously measure the deformation on all four free faces of the material. The practical execution of such an experiment is described by Guastavino and Göransson (2007). It is worth noting here that both the model described above and the measurements performed with the latter method are subjected to the assumption of linear deformations.

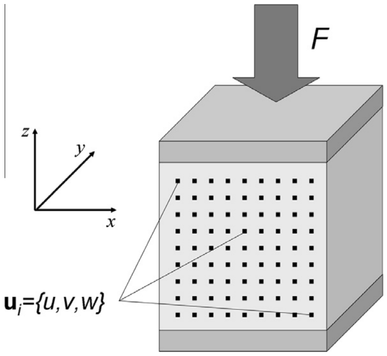

Fig. 1. Representation of the cubic sample (light grey) placed between two rigid plates (dark grey) with the coordinate system. The faces of each material are referred to as $x_-,\ x_+,\ y_-,\ y_+,\ z_-$ and z_+. The displacement is measured in a number of points on all free faces of the sample, here presented with 81 points on the y_- face.

A simplified representation of the setup is given in Fig. 1 for a compression of the material in the z direction. The material sample is placed in between two rigid plates. Note that the displacement is solely applied on the top plate and that the bottom plate stays stationary during the experiment. Therefore the frame of reference is the same for the compressed and uncompressed states and there is no rigid-body motion of the sample. The dimensions of the sample throughout this work are $100 \times 100 \times 100\,\text{mm}^3$. For ease of reference, the different faces of the cubic sample are indicated as $x_-,\ x_+,\ y_-,\ y_+,\ z_-,\ z_+$, with respect to the coordinate system defined for the sample. The displacement components are defined as $u = (x_0 - x_1),\ v = (y_0 - y_1)$ and $w = (z_0 - z_1)$, where $\{x_0, y_0, z_0\}$ and $\{x_1, y_1, z_1\}$ are the positions of a point in the material before and after compression respectively.

This experimental setup may easily be modelled with finite elements. The FE Model used here and in the further computations, is implemented within a conventional finite element package. The measured specimen is represented by a cubic sample of solid material. The boundary conditions are such that the displacement of the top of the material is equal to d_a in the direction of applied displacement, or longitudinal direction, and zero in the other two transverse directions. The displacements on the bottom face are all set equal to zero (fixed), and the other faces are unconstrained. The elements in the mesh are quadratic order Lagrange polynomial hexahedral elements. For this application, 10 elements per edge length of the sample are sufficiently accurate, which results in a total of 1000 elements. The model is solved for 27,783 DOFs.

An example of the deformation of the faces of a porous material is shown in Fig. 2 for a fictitious material with an isotropic Hooke's matrix, resulting from a compression of $d_a = 5$ mm in the z direction. In this example, the Hooke's matrix chosen is for an isotropic polyurethane open-cell foam with a Young's modulus $E = 70$ kPa, Poisson ratio $\nu = 0.39$ and hence a shear modulus $G = 25.18$ kPa (Hörlin & Göransson, 2000). As the material is isotropic, the same figures are found for compressions in the other directions. In Fig. 2, P is a parameter varying along the perimeter of the samples, the faces being represented from 0 m to 0.4 m in the order $[y_-, x_+, y_+, x_-]$ such that the edge at $P = (4 \times 0.1\ m) = 0.4$ m is the same edge as for $P = 0$ m. The second axis corresponds to the longitudinal coordinate, in this case the z axis, and the third axis presents the deformation. The longitudinal displacement component w is given in Fig. 2(c). It is equal for all faces, and it can be seen from the figure that the bottom of the material is indeed stationary ($w = 0$ mm for $z = 0$ m) and a compression of $d_a = 5$ mm is applied on the top ($w = -5$ mm for $z = 0.1$ m). Fig. 2(a) and (b) clearly show the effect of the positive Poisson ratio. There is no displacement component $u,\ v$ at the top and the bottom of the material, but the middle of the material has shifted outwards.

The target used in the inverse estimation, being the 3D displacement vector $\mathbf{u}^{\text{EXP}} = \{u, v, w\}$ at a number of N equidistant points, is extracted from each face of the material for each direction of compression. As the compression is applied parallel to all three coordinate axes this leads to a total of $12N$ data points per material containing information about the displacement in directions $x,\ y$ and z. In Fig. 1, an example is given of how the points may be distributed along one of the faces, with $N = 81$.

3.2. Optimisation space

The number of parameters to estimate in the inverse estimation may be reduced to eight due to the choice for the material deformation as target in the inverse estimation. One unique deformation pattern resulting from a static compression can be found for different stiffness matrices. Thus, for the inverse problem, multiple solutions for the Hooke's matrix are possible. However, only one unique normalised Hooke's tensor exists. This may be seen by considering the work per unit volume of the material. For two materials A and B of equal dimensions under compression, the work per unit volume is equal to $W_A = 1/2\underline{\boldsymbol{\varepsilon}}_A^T \mathbf{H}_A \underline{\boldsymbol{\varepsilon}}_A = \mathbf{F}_A \cdot \mathbf{u}_A$ and $W_B = 1/2\underline{\boldsymbol{\varepsilon}}_B^T \mathbf{H}_B \underline{\boldsymbol{\varepsilon}}_B = \mathbf{F}_B \cdot \mathbf{u}_B$, where $\mathbf{H}_A(B)$ represents the stiffness matrix (Jones, 1999), $\underline{\boldsymbol{\varepsilon}}_A(B)$ the strain vector, $\mathbf{u}_A(B)$ the deformations and $\mathbf{F}_A(B)$ the force needed to obtain deformation $\mathbf{u}_A(B)$ for material A and material B respectively. If the displacements of all points in materials A and B are equal ($\mathbf{u}_A = \mathbf{u}_B$) due to (not necessarily equal) forces $\mathbf{F}_A$ and $\mathbf{F}_B$ respectively, then the strain in these materials will also be equal ($\underline{\boldsymbol{\varepsilon}}_A = \underline{\boldsymbol{\varepsilon}}_B$), and consequently $W_A/W_B = \mathbf{H}_A/\mathbf{H}_B = \mathbf{F}_A/\mathbf{F}_B$. Thus a constant $C_H = \mathbf{F}_A/\mathbf{F}_B$ exists so that $\mathbf{H}_A = C_H \mathbf{H}_B$, and this constant can be found by measuring the force needed to obtain a certain deformation d_a.

The goal of the inverse estimation is thus to characterise the normalised Hooke's tensor, equal to the actual Hooke's tensor but for a constant factor C_H. If this constant factor is chosen such, that $H_{11}^{(0)} = 1$, the Hooke's matrix can be written as a multiplication of an initial guess matrix $\hat{H}_{ij}$ and a matrix of scaling constants H_{ij}^s, such that $H_{ij}^{(0)}/C_H = \hat{H}_{ij} \cdot H_{ij}^s$ with

$$\hat{\mathbf{H}} = \begin{bmatrix} 1 & \hat{H}_{12} & \hat{H}_{13} & 0 & 0 & 0 \\ & \hat{H}_{22} & \hat{H}_{23} & 0 & 0 & 0 \\ & & \hat{H}_{33} & 0 & 0 & 0 \\ & & & \hat{H}_{44} & 0 & 0 \\ & (\text{sym}) & & & \hat{H}_{55} & 0 \\ & & & & & \hat{H}_{66} \end{bmatrix} \tag{8}$$

and

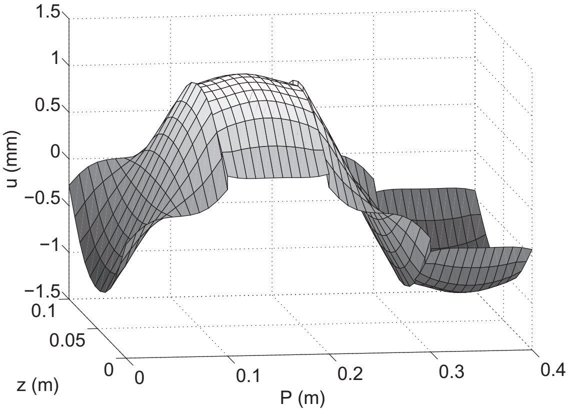

(a) u

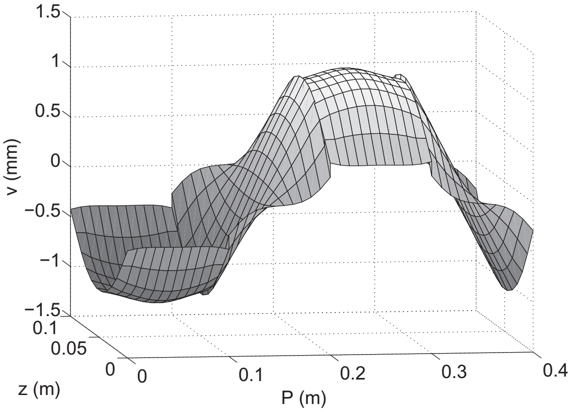

(b) v

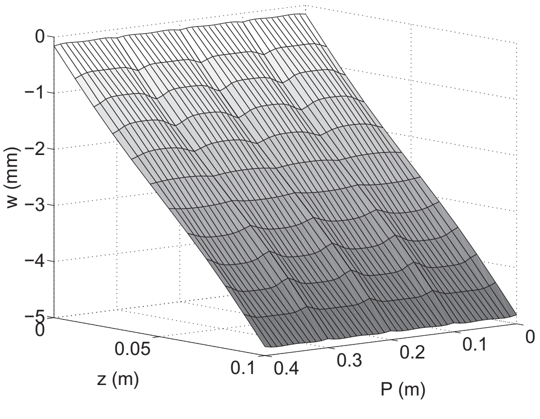

(c) w

Fig. 2. Deformation of fictitious isotropic porous material under static compression in *z*. Note that the figure (c) is rotated for clarity of the figure.

$$\mathbf{H}^s = \begin{bmatrix} 1 & \xi_3 & \xi_4 & 0 & 0 & 0 \\ & \xi_1 & \xi_5 & 0 & 0 & 0 \\ & & \xi_2 & 0 & 0 & 0 \\ & & & \xi_6 & 0 & 0 \\ & (\text{sym}) & & & \xi_7 & 0 \\ & & & & & \xi_8 \end{bmatrix}. \tag{9}$$

The angles $\alpha,\ \beta$ and γ are expressed as a multiplication of initial guesses with scaling constants,

$$\begin{aligned}\alpha &= \hat{\alpha}\cdot\xi_9,\\ \beta &= \hat{\beta}\cdot\xi_{10},\\ \gamma &= \hat{\gamma}\cdot\xi_{11}.\end{aligned} \tag{10}$$

The full optimisation space ξ_i thus contains 11 parameters,

$$\xi_i = [\,\xi_1 \quad \xi_2 \quad \xi_3 \quad \xi_4 \quad \xi_5 \quad \xi_6 \quad \xi_7 \quad \xi_8 \quad \xi_9 \quad \xi_{10} \quad \xi_{11}\,]^{\mathrm{T}}. \tag{11}$$

Certain restrictions are imposed on the Hooke's matrix $\mathbf{H}^{(0)}$ by the thermodynamic principle requiring that no energy can be created. This translates into a condition on the Hooke's matrix which must be positive definite and this is satisfied with the following constraints (Jones, 1999):

$$H_{ii}^{(0)} > 0, \quad i = 1,\ldots,6, \tag{12}$$

$$g_\sigma(\mathbf{H}^{(0)}) - 1 = 0, \quad \sigma = 1,\ldots,4, \tag{13}$$

where

$$\begin{aligned} &g_1 = \frac{\left(H_{23}^{(0)}\right)^2}{H_{22}^{(0)}H_{33}}, \quad g_2 = \frac{\left(H_{13}^{(0)}\right)^2}{H_{11}^{(0)}H_{33}^{(0)}}, \quad g_3 = \frac{\left(H_{12}^{(0)}\right)^2}{H_{11}^{(0)}H_{22}^{(0)}},\\ &g_4 = g_1 + g_2 + g_3 - 2\frac{H_{12}^{(0)}H_{23}^{(0)}H_{31}^{(0)}}{H_{11}^{(0)}H_{22}^{(0)}H_{33}^{(0)}}. \end{aligned} \tag{14}$$

In addition, the following constraints apply to the angles α, β and γ,

$$-\pi/2 < \alpha, \quad \beta, \quad \gamma < \pi/2. \tag{15}$$

3.3. Inverse estimation

In the inverse estimation procedure, a material model is varied to approximate the measured displacements. In each iteration of the optimisation routine, a finite element model representing the experimental setup is solved for a proposed set of constitutive parameters, Eq. (11). An important assumption made here is that the frame of the porous material is assumed to behave as an equivalent solid as the influence of pressure variations in the air can be neglected under a slow loading (Hörlin & Göransson, 2010). For one full calculation of the displacements, three FEM solutions are computed for $x,\ y$ and z directions. From these, the displacements $\boldsymbol{u}^{\mathrm{FE}}(\xi_i) = \{u, v, w\}$ are extracted at the same points as in the experiment. The difference between measured and simulated displacements is the basis for the objective function, defined as the square of the absolute difference between the predicted displacements and the measured displacements, summed over all faces f in each compression direction c for all points per face N,

$$f(\xi_i) = 1 + A\sum_{c=1}^{3}\sum_{f=1}^{4}\sum_{k=1}^{N}\left|{}_f^c u_k^{\mathrm{FE}}(\xi_i) - {}_f^c u_k^{\mathrm{EXP}}\right|^2. \tag{16}$$

In the calculation of the objective function, a term 1 and a multiplication factor A are added for numerical stability. As the displacement applied is in mm, the factor A is chosen to be a scaling parameter equal to 10^3. Another possibility is to choose $A = |1/d_{\mathrm{a}}|$, as the inverse of the applied displacement.

At this point it is important to note that a particular strength of the method lies in the fact that the inverse estimation procedure is performed by comparing experimental and simulated displacements, which avoids errors often encountered in the estimation of strains from experimental displacements (Průša, Rajagopal, & Saravanan, 2013).

The optimisation routine is implemented in Matlab using the globally convergent method of moving asymptotes (GCMMA) by Svanberg (2002). The GCMMA routine pursues a strict decrease of the object function, guaranteeing a set of parameters which is a preferable solution. A detailed description of the GCMMA algorithm is given in the original paper by Svanberg (2002). The criteria to assess whether the optimisation is converged are that a variation in the objective function and in each of the parameters must be less than 10^{-4} between two subsequent iterations.

To get an understanding of how the differences between simulated and measured displacements are spread, a symbolic representation of the measure of this difference is given for each compression direction c,

$$\boldsymbol{\mu}_m^c = \frac{1}{N}\sum_{f=1}^{4}\sum_{k=1}^{N}\left|\frac{{}_f\boldsymbol{u}_k^{\mathrm{FE}}(\xi_i) - {}_f\boldsymbol{u}_k^{\mathrm{EXP}}}{d_{\mathrm{a}}}\right|, \tag{17}$$

which can be written as a matrix,

$$\boldsymbol{\mu}_m = \begin{bmatrix} \mu_{\mathrm{u,x}} & \mu_{\mathrm{v,x}} & \mu_{\mathrm{w,x}} \\ \mu_{\mathrm{u,y}} & \mu_{\mathrm{v,y}} & \mu_{\mathrm{w,y}} \\ \mu_{\mathrm{u,z}} & \mu_{\mathrm{v,z}} & \mu_{\mathrm{w,z}} \end{bmatrix}. \tag{18}$$

The component $\mu_{\mathrm{u,x}}$ for example gives the average difference on the displacement components u for compression in the x direction over all four faces, relative to the applied displacement d_{a}. Note that the subscript m has been introduced in order to identify the results for the different samples tested and discussed in later sections.

4. Validation of the inverse estimation approach

The method proposed here for characterisation of the static Hooke's tensor of orthotropic porous materials is verified for four artificial materials with a priori known elastic properties. The method will subsequently be applied to an isotropic foam, a transversely isotropic and an orthotropic material, and a rotated generally orthotropic foam. A numerical experiment is conducted to this end for a compression $d_{\mathrm{a}} = 5$ mm, in order to evaluate the ability of the approach to estimate the Hooke's matrix to an acceptable degree of accuracy for different material symmetries and for different ranges of the values in the Hooke's matrix. For each material, the displacements are numerically generated, and then used as targets in the inverse estimation. Recall that the numerically generated displacements will be referred to as the measured displacements. To verify the generality of the approach, the known material symmetry is not taken into account in the inverse estimation, and each material is addressed as if it were orthotropic.

The starting point for the optimisation can be chosen arbitrarily, and the final solution does not depend on the chosen starting point. This was verified by repeating the inverse estimation for different starting points, converging each time towards the same optimum. The results shown are for an initial guess with the non-zero elements of $\hat{H}_{ij} = 1$, see Eq. (8), and the initial choice for the scaling constants

$$\xi_i = [1 \quad 1 \quad 0.4286 \quad 0.4286 \quad 0.4286 \quad 0.2857 \quad 0.2857 \quad 0.2857\,]^{\mathrm{T}}, \tag{19}$$

representing an isotropic Hooke's matrix with arbitrary Young's modulus and a Poisson ratio of $\nu = 0.30$. An isotropic starting point was selected, since there is sometimes data available on the isotropic elastic moduli of the porous material in the literature.

In order to test another aspect of the generality of the approach the bounds for the parameters are chosen very large, imposing no restrictive assumption on the values of the parameters. The allowed minimum and maximum values in the optimisation are given in Eq. (20). The lower limit is set to a value $C_{\mathrm{L}} = 0.0005$, different from zero for numerical stability reasons,

$$\begin{aligned} \xi_{i,\min} &= [C_{\mathrm{L}} \quad C_{\mathrm{L}} \quad -50 \quad -50 \quad -50 \quad C_{\mathrm{L}} \quad C_{\mathrm{L}} \quad C_{\mathrm{L}}]^{\mathrm{T}}, \\ \xi_{i,\max} &= [100 \quad 100 \quad 50 \quad 50 \quad 50 \quad 100 \quad 100 \quad 100]^{\mathrm{T}}. \end{aligned} \tag{20}$$

The error measure used in order to validate the proposed method is given by

$$\epsilon = \frac{|\boldsymbol{x}_{\mathrm{opt}} - \boldsymbol{x}_{\mathbf{0}}|}{\boldsymbol{x}_{\mathbf{0}}}, \tag{21}$$

where $\boldsymbol{x}_{\mathbf{0}}$ are the values of the parameters for the target material (here used for the fictitious measurements), and $\boldsymbol{x}_{\mathrm{opt}}$ are the values of the parameters which give the best fit of the model, resulting from the inverse estimation.

4.1. Properties of artificial materials studied

Four artificial materials are studied in order to verify the applicability of the method. In order to show the feasibility of the approach, its limits are investigated. Therefore the fictitious materials used in the verification are rather extreme cases. A material with a large ratio between in-plane and out-of-plane in the transversely isotropic case is selected to this end. In the orthotropic case as well, a Hooke's tensor was chosen which would be challenging for the inverse characterisation method.

The properties of the fictitious isotropic material are obtained from Hörlin and Göransson (2000), and were presented earlier. The fictitious transversely isotropic tensor is fully defined by five parameters. The data for the elastic and shear moduli are taken from a previously reported fibrous material (Rice & Göransson, 1999). The out of plane moduli are E_{x} and G_{yz}, and the in-plane moduli are $E_{\mathrm{y,z}}$ and $G_{\mathrm{zx,xy}}$. The Poisson ratio ν_{zy} is obtained from the relation $1/G_{\mathrm{yz}} = 2(1 + \nu_{\mathrm{zy}})/E_{\mathrm{y}}$. The Poisson ratio $\nu_{\mathrm{yx}} = \nu_{\mathrm{zx}}$ was chosen within certain limits such that the Hooke's matrix would be positive definite. The third case investigated is an orthotropic material. Little literature is available on the elastic properties of orthotropic porous materials. The composed artificial Hooke's matrix has a large ratio between smallest and largest moduli, one Poisson ratio (ν_{zy}) is close to zero, and one Poisson ratio (ν_{xz}) close to the possible limit for positive definiteness. The last case also includes a transformation of the Hooke's matrix $\mathbf{H}^{(0)}$ to give the Hooke's matrix $\mathbf{H}^{(0)}_{\mathrm{a}}$, see Eq. (5). The rotations are arbitrarily chosen as $\pi/10$ radians around the x axis, $-\pi/6$ radians around the y axis and $\pi/36$ radians around the z axis.

A complete overview of the properties, in terms of engineering constants, of the four fictitious materials used for the verification of the method are presented in Table 1.

4.2. Isotropic material

The first verification case is performed for the isotropic material. The material data may be found in Table 1. The deformations for this artificial material are given in Fig. 2 for a compression $d_a = 5$ mm in the z direction.

The actual Hooke's matrix, and the engineering constants can be calculated from the non-dimensional variables in the optimal solution. The average force (over all three directions) $\hat{F}^{\mathrm{EXP}}$ needed to compress the fictitious material in the numerical experiment by $d_a = 5$ mm equals -38.77 N. The average force $\hat{F}^{\mathrm{FE}}$ needed for a compression of a material with Hooke's tensor $H_{ij}^{(0)}/C_{\mathrm{H}}$ equals $-0.277 \cdot 10^{-3}$N. The actual Hooke's tensor is then obtained by multiplying the dimensionless Hooke's matrix with the constant $C_{\mathrm{H}} = \hat{F}^{\mathrm{EXP}}/\hat{F}^{\mathrm{FE}} = 139.891 \cdot 10^3$. The target and estimated engineering constants are given in Table 2 together with their relative difference.

The iteration history of the objective function is shown in Fig. 3 (omitting the added constant) and the corresponding convergence of the different scaling constants is shown in Fig. 4.

The relative average difference in the displacements for the optimal solution, i.e. the components corresponding to Eq. (18), is

$$\boldsymbol{\mu}_{\mathrm{iso}} = \begin{bmatrix} 0.0054 & 0.0241 & 0.0241 \\ 0.0360 & 0.0088 & 0.0186 \\ 0.0360 & 0.0186 & 0.0088 \end{bmatrix} (\%). \tag{22}$$

4.3. Transversely isotropic material

The second verification case is the fictitious transversely isotropic material, of which the properties can be found in Table 1. The deformations resulting from a compression of $d_a = 5$ mm are shown in Fig. 5 for three displacement–compression cases. Fig. 5(a) shows the displacement component v resulting from a compression in x, Fig. 5(b) and (c) show the displacement component u and w respectively for a compression in y. The effect of transverse isotropy in the longitudinal direction, e.g. displacement component w in direction z, is not shown here as it is perceived to a lesser extent, since the deformation of the top of the material must be equal to d_a and the deformation of the bottom must be zero.

In Fig. 5(a), which shows compression along the x axis, P is once again a parameter varying along the perimeter of the samples, the faces being shown from 0 m to 0.4 m in the order $[z_-, y_+, z_+, y_-]$ so that the edge at $P = 0.4$ m is the same edge as $P = 0$ m. The second axis is the longitudinal coordinate, in this case the x axis and the third axis presents the deformation. For Fig. 5(b) and (c), the axis of compression is the y axis, and the faces are shown in the order $[x_-, z_+, x_+, z_-]$.

The effect of the Poisson ratio can be clearly seen in Fig. 5. In Fig. 5(a), the Poisson ratio $\nu_{xy} = \nu_{xz}$ results in a low but outward and thus positive (negative) displacement component v for face $y_+(y_-)$. The displacement component w for a compression in x gives the same result. Fig. 5(b) shows a large outward displacement component v or w due to the Poisson ratio $\nu_{yx} = \nu_{zx}$. The displacement profile as a result of a negative Poisson ratio is seen in Fig. 5(c), giving a negative (positive) displacement component w for face $z_+(z_-)$, oriented inwards.

The Hooke's matrix for the optimal solution is calculated from the average force needed to compress the foam by d_a in all three directions, as was more elaborately shown for the isotropic case. Table 3 gives the engineering constants for the optimal solution and the relative difference between these and the target engineering constants.

The iteration history of the objective function is shown in Fig. 6 (omitting the added constant), and the corresponding convergence of the different scaling constants is shown in Fig. 7.

Table 1
Engineering constants for artificial materials.

Eng. const.	Isotropic	Transverse isotropic	Orthotropic	Anisotropic
E_x [kPa]	70	0.225	300	300
E_y [kPa]	70	17.2	217	217
E_z [kPa]	70	17.2	78	78
ν_{yx} [-]	0.39	4	0.5	0.5
ν_{xz} [–]	0.39	0.0523	-1.55	-1.55
ν_{zy} [–]	0.39	-0.3723	0.1	0.1
G_{yz} [kPa]	25.18	13.7	140	140
G_{zx} [kPa]	25.18	1.2	60	60
G_{xy} [kPa]	25.18	1.2	440	440
α[–]	0	0	0	$\pi/10$
β [–]	0	0	0	$-\pi/6$
γ [–]	0	0	0	$\pi/36$

Table 2
Comparison of the engineering constants for the target and optimal solution for fictitious isotropic material.

$\boldsymbol{x}$	$\boldsymbol{x}_0$	$\boldsymbol{x}_{\mathrm{opt}}$	$\frac{\lvert \boldsymbol{x}_{\mathrm{opt}} - \boldsymbol{x}_0 \rvert}{\boldsymbol{x}_0}$ (%)
E_x [Pa]	70,000	70,308	0.44
E_y [Pa]	70,000	69,924	0.11
E_z [Pa]	70,000	69,924	0.11
ν_{yx} [–]	0.39	0.389	0.06
ν_{xz} [–]	0.39	0.391	0.22
ν_{zy} [–]	0.39	0.390	0.03
G_{yz} [Pa]	25180	24,994	0.74
G_{zx} [Pa]	25180	24,937	0.97
G_{xy} [Pa]	25180	24,937	0.97

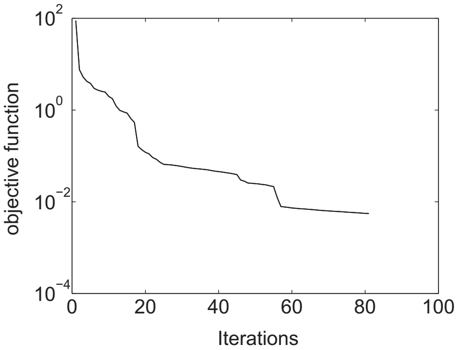

Fig. 3. Iteration history of objective function for fictitious isotropic material.

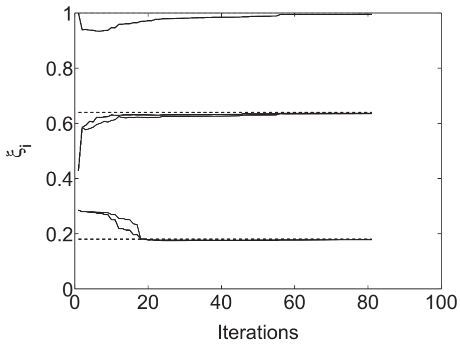

Fig. 4. Iteration history of scaling constants ξ_i for fictitious isotropic material, dashed line being the target.

The relative average difference in the displacement for the optimal solution, i.e. the components corresponding to Eq. (18), is

$$\boldsymbol{\mu}_{\mathrm{trans}} = \begin{bmatrix} 0.0011 & 0.0038 & 0.0040 \\ 0.0057 & 0.0062 & 0.0063 \\ 0.0060 & 0.0061 & 0.0063 \end{bmatrix} (\%). \tag{23}$$

4.4. Orthotropic material

The engineering constants of the chosen Hooke's tensor are given in Table 1. The effect of the Poisson ratio, which has been shown previously for the isotropic and transversely isotropic materials, is clear from Figs. 2 and 5. A figure representing the displacements of this material under compression is therefore not given, as it would not add any further information. On the other hand, the effect of the shear moduli on the displacement due to a compression is shown here. For a material with a Hooke's tensor with engineering constants used here, the maximum displacement component $v_{\max}$ due to a compression in x

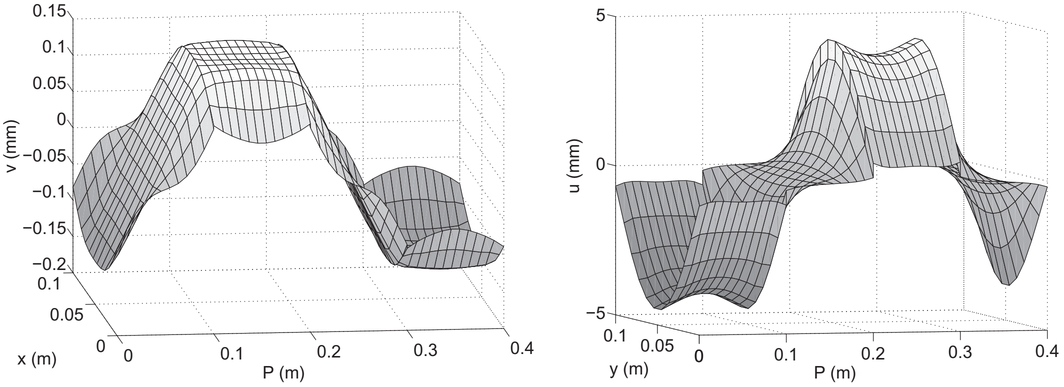

(a) v due to compression in x (b) u due to compression in y

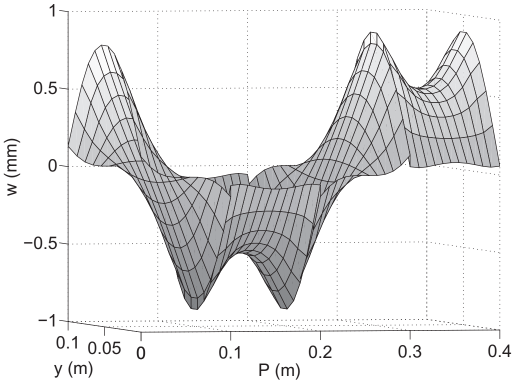

(c) w due to compression in y

Fig. 5. Deformation of transversely isotropic porous material under static compression d_a.

Table 3
Comparison of the engineering constants for the target and optimal solution for fictitious transversly isotropic material.

$\boldsymbol{x}$	$\boldsymbol{x_0}$	$\boldsymbol{x}_{\text{opt}}$	$\frac{\lvert \boldsymbol{x}_{\text{opt}} - \boldsymbol{x_0} \rvert}{\boldsymbol{x_0}}$ (%)
E_x [Pa]	225	225.4	0.17
E_y [Pa]	17,200	17,183	0.10
E_z [Pa]	17,200	17,181	0.11
ν_{yx} [–]	4	4.00	0.06
ν_{xz} [–]	0.0523	0.0524	0.22
ν_{zy} [–]	−0.3723	−0.3722	0.03
G_{yz} [Pa]	13,700	13,557	1.05
G_{zx} [Pa]	1200	1202.0	0.17
G_{xy} [Pa]	1200	1202.1	0.17

is equal to 2.4 μm while for a material with an identical Hooke's matrix, except for $G_{xy} = 140$ kPa, the maximum displacement component $v_{\max}$ equals 1.9 μm. This coupling between compression and shear is important and allows to identify the shear moduli in the proposed approach.

The Hooke's matrix for the optimal solution is calculated from the average of the force needed to compress the foam by d_a in all three directions, as done for the isotropic case. Table 4 gives the engineering constants for the optimal solution and the relative difference between these and the target engineering constants.

The iteration history of the objective function is shown in Fig. 8 (omitting the added constant), and the corresponding convergence of the different scaling constants is shown in Fig. 9.

The relative average difference in the displacement for the optimal solution, i.e. the components corresponding to Eq. (18), is

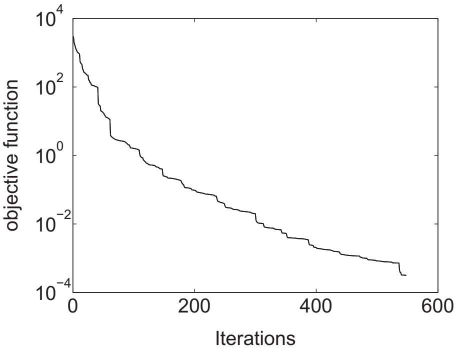

Fig. 6. Iteration history of objective function for fictitious transversely isotropic material.

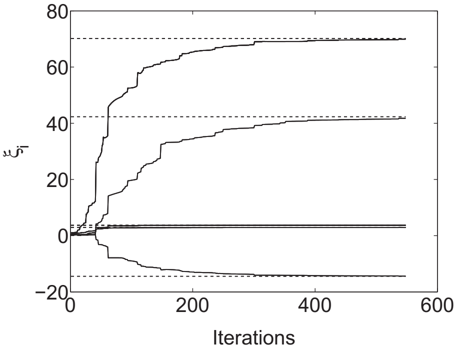

Fig. 7. Iteration history of scaling constants ξ_i for fictitious transversely isotropic material, dashed line being the target.

$$\boldsymbol{\mu}_{\text{ortho}} = \begin{bmatrix} 0.048 & 0.046 & 0.043 \\ 0.061 & 0.034 & 0.086 \\ 0.22 & 0.035 & 0.049 \end{bmatrix} (\%). \tag{24}$$

4.5. Generally orthotropic material

The last case studied is the generally orthotropic material, with 21 components in the Hooke's matrix. In order to find a converged solution, different strategies for the inverse estimation have been evaluated. The computationally most effective approach was found to consist of two phases. In the first phase, an inverse estimation is executed with parameters ξ_1 to ξ_8, with the angles equal to zero during this phase. When the stop criteria are fulfilled for the first phase, with parameters ξ^1_{1-8} as outcome, a new inverse estimation is initialised with all parameters active, and as a starting point for parameters ξ_1 to ξ_8 the results ξ^1_{1-8} of the previous phase.

Table 5 shows the target and estimated engineering constants, together with their relative difference.

Table 4
Comparison of the engineering constants for the optimal solution for fictitious orthotropic material.

$\boldsymbol{x}$	$\boldsymbol{x_0}$	$\boldsymbol{x}_{\text{opt}}$	$\frac{\lvert\boldsymbol{x}_{\text{opt}}-\boldsymbol{x_0}\rvert}{\boldsymbol{x_0}}$ (%)
E_x [Pa]	300,000	297,158	0.95
E_y [Pa]	217,000	215,657	0.62
E_z [Pa]	78,000	78,825	1.06
ν_{yx} [−]	0.5	0.50	0.15
ν_{xz} [−]	−1.55	−1.54	0.62
ν_{zy} [−]	0.1	0.10	0.37
G_{yz} [Pa]	140,000	143,387	2.42
G_{zx} [Pa]	60,000	59,751	0.41
G_{xy} [Pa]	440,000	433,510	1.48

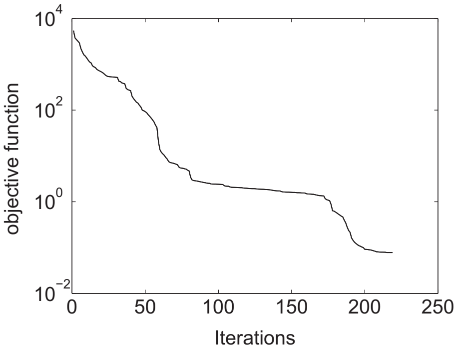

Fig. 8. Iteration history of objective function for fictitious orthotropic material.

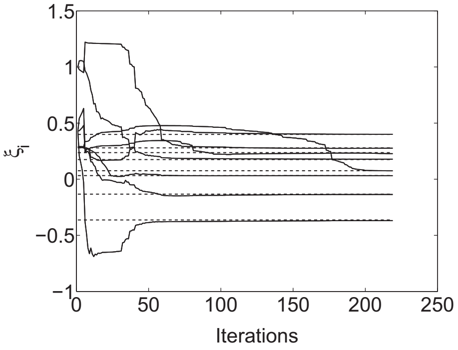

Fig. 9. Iteration history of scaling constants ξ_i for fictitious orthotropic material, dashed line being the target.

Table 5
Comparison of the engineering constants for the optimal solution for fictitious generally orthotropic material.

$\boldsymbol{x}$	$\boldsymbol{x_0}$	$\boldsymbol{x}_{\text{opt}}$	$\frac{\lvert\boldsymbol{x}_{\text{opt}}-\boldsymbol{x_0}\rvert}{\boldsymbol{x_0}}$ (%)
E_1 [Pa]	300,000	302,409	0.80
E_2 [Pa]	217,000	217,697	0.32
E_3 [Pa]	78,000	77,084	1.17
ν_{21} [-]	0.5	0.50	0.30
ν_{13} [-]	-1.55	−1.55	0.11
ν_{32} [-]	0.1	0.099	1.30
G_{23} [Pa]	140,000	139,560	0.31
G_{31} [Pa]	60,000	59531	0.78
G_{12} [Pa]	440,000	443,276	0.75

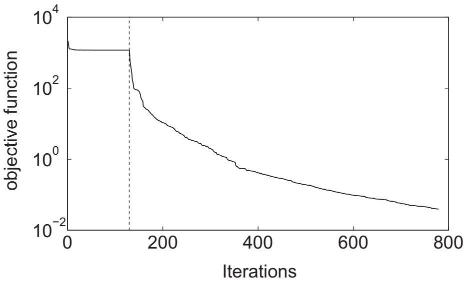

Fig. 10. Iteration history of objective function for fictitious generally orthotropic material.

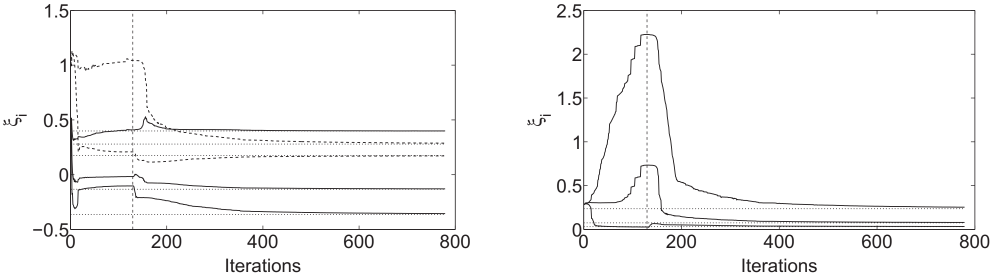

(a) $\xi_i, i = 1, 2$ - dashed line; $i = 3, \ldots, 5$ - solid line.

(b) $\xi_i, i = 6, \ldots, 8$.

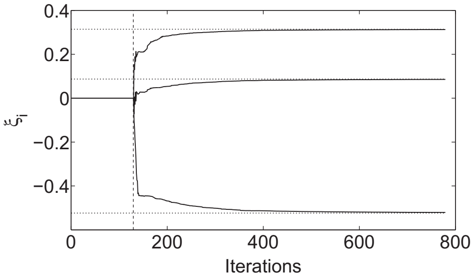

(c) $\xi_i, i = 9, \ldots, 11$.

Fig. 11. Iteration history of scaling constants ξ_i for fictitious generally orthotropic material, dotted line being the target. The vertical line marks the end of phase 1 and the beginning of phase 2. Parameters ξ_{9-11} are activated in phase 2 only.

The iteration history of the objective function is shown in Fig. 10 (omitting the added constant). The vertical line indicates the point in the simulation where the optimisation has converged for phase 1 and is initialised for the succeeding phase. The corresponding convergence of the scaling constants is shown in Fig. 11. In the first phase, the angles are not activated in the inverse estimation and hence are equal to zero.

The relative average difference in the displacement for the optimal solution, i.e. the components corresponding to Eq. (18), is given (in percent) in Eq. (25),

$$\boldsymbol{\mu}_{\text{an}} = \begin{bmatrix} 0.083 & 0.040 & 0.071 \\ 0.043 & 0.057 & 0.070 \\ 0.063 & 0.019 & 0.071 \end{bmatrix} (\%). \qquad (25)$$

5. Discussion

The proposed characterisation method is verified for four fictitious materials with different degrees of anisotropy. The artificial stiffness matrices are retrieved with a good accuracy. For all cases, the objective function decreases monotonically, as is expected for the optimisation algorithm used.

For the isotropic material, the difference between the target and optimal values of the engineering constants is small. The inverse estimation converges in a relatively small number of iterations, since the starting point is an isotropic matrix. Note that, although the material is isotropic, the optimal Hooke's tensor deviates slightly from isotropy, as a result of imposing that $H_{11}^{(0)} = 1$. Since $H_{22}^{(0)}$ and $H_{33}^{(0)}$ are not converged to exactly 1, perfect isotropy is not reached. If the inverse estimation would have been allowed to continue for more iterations, full convergence and perfect isotropy would be reached. On the other hand, a real material most probably will never assume a perfect isotropic symmetry. The differences between targeted and optimal parameters are largest for the parameters related to the shear moduli, since they have the smallest influence on the displacements resulting from a compression. The relative average difference in displacement between experiment and simulation, Eq. (22), is smaller than 0.05%, and is smallest for the longitudinal displacement components, i.e. $\mu_{\text{u,x}}$, $\mu_{\text{v,y}}$, $\mu_{\text{w,z}}$.

The convergence of the transversely isotropic fictitious material takes considerably more iterations. This is due to the rather extreme transverse isotropy of the chosen material. The scaling constants are very large as the ratio between in-plane and out-of-plane elastic moduli is very high. Nevertheless, the target properties are obtained with very good accuracy. For this case, the relative average difference in displacement, Eq. (23), is very small for all components. This case shows that a very large ratio between the different engineering constants should not cause a problem for the characterisation method.

The orthotropic case converged with good accuracy as well. The convergence for the scaling constants is not as smooth as for the other fictitious materials. The scaling constant ξ_6 only converges when all other parameters have converged. This is possibly due to the low Poisson ratio ν_{zy} chosen in this case, which results in a limited coupling between the shear moduli and the elastic moduli. In the optimiser, the objective function is not very sensitive to changes in this shear modulus. This might point to a potential problem of the approach when studying materials with very small Poisson ratios. The relative average difference in displacement is less than 0.1%, except for the component $\mu_{u,z}$.

The result for the generally orthotropic case shows that the method retrieves the angles and the engineering constants with very good accuracy. The relative differences in the displacement between the optimal and the target solution, given by Eq. (24), are all very small as well. This numerical example confirms that the computational part of the inverse estimation works accurately, for data free from various flaws, such as noise or uncertainty due to geometry, mounting and inhomogeneity.

The verification performed intends to show the generality with which the method may be applied. Therefore the starting point and the bounds for the parameters have been chosen in such a way that no restrictive assumptions on the values of the parameters were imposed. If these were to be chosen with a certain a priori knowledge and if the number of iterations would be increased, the optimal values in the inverse estimation would be even closer to the target values. However, the result in this paper is satisfactory and shows that the approach gives good results for estimating the static Hooke's matrix of orthotropic materials.

6. Robustness of the method

To conclude the study of the computational part of the characterisation method, the robustness of the method was studied for the rotated orthotropic material verified in the previous section. Two aspects of the robustness are studied. First, an uncertainty is added to the experiment, i.e. the input displacement in one of the directions is increased by 10%. A second study shows the effect of uncertainties in the sample dimensions on the inverse estimation results.

6.1. Sensitivity to uncertainty on input displacement

The compression d_a is changed in the z direction from 5 to 5.5 mm in the numerical experiment. In the inverse estimation, it is assumed that the displacement in all directions is 5 mm. Table 6 gives the target values for the engineering parameters, the optimal values found for the case with uncertainty, and the relative difference between both.

The relative average difference between the displacement for the optimal solution and the target without uncertainties, i.e. the components corresponding to Eq. (18), is given (in percent) in Eq. (26),

$$\boldsymbol{\mu}_{d_a} = \begin{bmatrix} 0.24 & 0.27 & 0.27 \\ 0.19 & 0.17 & 0.13 \\ 0.38 & 0.24 & 0.62 \end{bmatrix} (\%). \tag{26}$$

These results show that an uncertainty of 10% on the compression, results in a smaller difference in the engineering constants. Of course, some parameters are affected more than others, but the final difference for all is still less than the uncertainty of 10% introduced in the input. From Eq. (26), it may be possible to see where the error has occurred. The relative average difference for the compression in z direction is larger than in the other directions.

6.2. Sensitivity to uncertainties on sample dimensions

The sample size is adjusted from $100 \times 100 \times 100\ \text{mm}^3$ to $95 \times 95 \times 95\ \text{mm}^3$ in the numerical experiment. This corresponds to a change in volume of approximately 12%. In the inverse estimation it is assumed that the sample size is $100 \times 100 \times 100\ \text{mm}^3$. Table 7 gives the target values for the engineering parameters, the optimal values found for the case with uncertainty, and the relative difference between both.

Table 6

Comparison of the engineering constants and angles for the optimal solution with uncertainty on input displacement.

$\boldsymbol{x}$	$\boldsymbol{x_0}$	$\boldsymbol{x}_{\text{opt}}$	$\frac{\lvert \boldsymbol{x}_{\text{opt}} - \boldsymbol{x_0} \rvert}{\boldsymbol{x_0}}$ (%)
E_1 [Pa]	300,000	296,044	1.32
E_2 [Pa]	217,000	229,733	5.87
E_3 [Pa]	78,000	77,560	0.56
ν_{21} [–]	0.5	0.52	3.77
ν_{13} [–]	−1.55	−1.56	0.91
ν_{32} [–]	0.1	0.10	3.96
G_{23} [Pa]	140,000	151,897	8.50
G_{31} [Pa]	60,000	63,047	5.08
G_{12} [Pa]	440,000	455,463	3.51
α (rad)	0.3142	0.3183	1.33
β (rad)	−0.5236	−0.5254	0.33
γ (rad)	0.0873	0.093	6.61

Table 7
Comparison of the engineering constants and angles for the optimal solution, with uncertainties on sample dimensions.

$\boldsymbol{x}$	$\boldsymbol{x_0}$	$\boldsymbol{x}_{\text{opt}}$	$\frac{\lvert \boldsymbol{x}_{\text{opt}} - \boldsymbol{x_0} \rvert}{\boldsymbol{x_0}}$ (%)
E_1 [Pa]	300,000	277,405	7.53
E_2 [Pa]	217,000	200,294	7.70
E_3 [Pa]	78,000	74,724	4.2
ν_{21} [−]	0.5	0.51	1.95
ν_{13} [−]	−1.55	−1.57	1.59
ν_{32} [−]	0.1	0.11	10.48
G_{23} [Pa]	140,000	142,167	1.55
G_{31} [Pa]	60,000	58,265	2.89
G_{12} [Pa]	440,000	438,610	0.32
α (rad)	0.3142	0.3112	0.94
β (rad)	−0.5236	−0.5319	1.59
γ (rad)	0.0873	0.090	2.66

The relative average difference between the displacement for the optimal solution and the target without uncertainty, i.e. the components corresponding to Eq. (18), is given (in percent) in Eq. (27),

$$\boldsymbol{\mu}_{\text{dim}} = \begin{bmatrix} 0.57 & 0.20 & 0.33 \\ 0.32 & 0.49 & 0.24 \\ 0.24 & 0.11 & 0.32 \end{bmatrix} (\%). \tag{27}$$

The difference in the engineering constants is again smaller than the uncertainty on the sample dimensions. The Young's moduli are most sensitive to the uncertainties introduced, and are consistently smaller than the original values, as expected. The effect on the angles is small. From Eq. (27), it can be seen that the sensitivity is largest in the direction of compression, i.e. the diagonal elements of this matrix.

7. Conclusion

This paper investigates the feasibility of an approach for the characterisation of the static Hooke's tensor of a porous material. The data used as input to the inverse estimation are measurements of the displacements on the faces of the material when compressed along the three coordinate axes. The proposed approach establishes a normalised Hooke's matrix for a cubic sample of porous material, and the actual values may be found by measuring the force applied on the material. An objective function is proposed, based on the relative difference between measured and simulated displacements $\mathbf{u}^{\text{EXP}}$ and $\mathbf{u}^{\text{FE}}$ in the three directions of compression.

As a validation of the approach, the method is applied to four artificial porous materials with different degrees of anisotropy and different values for the engineering constants. The implications of anisotropy on the displacements are discussed and illustrated. The a priori known Hooke's matrix is retrieved with good accuracy for each test case, which shows that the approach is valid and may be applied to real materials to obtain the static Hooke's tensor of a porous material. The investigation in this paper also shows that caution is needed when studying materials of which the Poisson ratio is close to zero, due to the low shear coupling. The proposed numerical approach is also studied for its robustness, where it is seen that the effect of perturbations on the input data is smaller than the perturbation itself.

Experimental considerations have not been included in the present paper. A forthcoming paper will be devoted to the application of the method to a real industrial porous material.

Acknowledgements

The authors would like to acknowledge the support from the European Union, the Smart Structures Project (Contract No. MRTN-CT-2006-035559), under which part of the research has been performed.

Appendix A. Transformation for Hooke's matrix

The Bond matrix for transformation of the Hooke's matrix in Eq. (5) is given by Slawinski (2010) and Carcione (2007)

$$\mathbf{A}_{\varepsilon} = \begin{bmatrix} \mathbf{A}_{11} & \mathbf{A}_{12} \\ \mathbf{A}_{21} & \mathbf{A}_{22} \end{bmatrix}, \tag{A.1}$$

where

$$\begin{aligned}
\mathbf{A}_{11} &= \begin{bmatrix} a_{11}^2 & a_{12}^2 & a_{13}^2 \\ a_{21}^2 & a_{22}^2 & a_{23}^2 \\ a_{31}^2 & a_{32}^2 & a_{33}^2 \end{bmatrix}, \\
\mathbf{A}_{12} &= \begin{bmatrix} a_{12}a_{13} & a_{11}a_{13} & a_{11}a_{12} \\ a_{22}a_{23} & a_{21}a_{23} & a_{21}a_{22} \\ a_{32}a_{33} & a_{31}a_{33} & a_{31}a_{32} \end{bmatrix}, \\
\mathbf{A}_{21} &= \begin{bmatrix} 2a_{21}a_{31} & 2a_{22}a_{32} & 2a_{23}a_{33} \\ 2a_{11}a_{31} & 2a_{12}a_{32} & 2a_{13}a_{33} \\ 2a_{11}a_{21} & 2a_{12}a_{22} & 2a_{13}a_{23} \end{bmatrix}, \\
\mathbf{A}_{22} &= \begin{bmatrix} a_{22}a_{33}+a_{23}a_{32} & a_{21}a_{33}+a_{23}a_{31} & a_{21}a_{32}+a_{22}a_{31} \\ a_{12}a_{33}+a_{13}a_{32} & a_{11}a_{33}+a_{13}a_{31} & a_{11}a_{32}+a_{12}a_{31} \\ a_{12}a_{23}+a_{13}a_{22} & a_{11}a_{23}+a_{13}a_{21} & a_{11}a_{22}+a_{12}a_{21} \end{bmatrix}.
\end{aligned} \tag{A.2}$$

The entries a_{ij} are the elements of transformation matrix $\mathbf{A}_\varepsilon$, defined by a successive rotation around the fixed x, y, and z axes of the natural coordinate system by angles α, β and γ respectively,

$$\mathbf{a} = \mathbf{R}(x,\alpha)\ \mathbf{R}(y,\beta)\ \mathbf{R}(z,\gamma) = \begin{bmatrix} a_{11} & a_{12} & a_{13} \\ a_{21} & a_{22} & a_{23} \\ a_{31} & a_{32} & a_{33} \end{bmatrix}, \tag{A.3}$$

with

$$\mathbf{R}(x,\alpha) = \begin{bmatrix} 1 & 0 & 0 \\ 0 & \cos\alpha & \sin\alpha \\ 0 & -\sin\alpha & \cos\alpha \end{bmatrix}, \quad \mathbf{R}(y,\beta) = \begin{bmatrix} \cos\beta & 0 & -\sin\beta \\ 0 & 1 & 0 \\ \sin\beta & 0 & \cos\beta \end{bmatrix}, \tag{A.4}$$

$$\mathbf{R}(z,\gamma) = \begin{bmatrix} \cos\gamma & \sin\gamma & 0 \\ -\sin\gamma & \cos\gamma & 0 \\ 0 & 0 & 1 \end{bmatrix}. \tag{A.5}$$

References

Biot, M. A. (1954). Theory of stress–strain relations in anisotropic viscoelasticity and relaxation phenomena. *Journal of Applied Physics, 25*, 1385–1391.

Biot, M. A. (1956). Theory of propagation of elastic waves in a fluid-saturated porous solid. 1. Low-frequency range. *Journal of the Acoustical Society of America, 26*, 168–178.

Carcione, J. M. (2007). *Wave fields in real media: Wave propagation in anisotropic, anelastic, porous media and electromagnetic media* (2nd ed.). Elsevier Science [p. 515].

Cuenca, J., & Göransson, P. (2012). Inverse estimation of the elastic and anelastic properties of the porous frame of anisotropic open-cell foams. *Journal of the Acoustical Society of America, 132*, 621–629.

Cuenca, J., Van der Kelen, C., & Göransson, P. (2014). A general methodology for inverse estimation of the elastic and anelastic properties of anisotropic open-cell porous materials – With application to a melamine foam. *Journal of Applied Physics, 115*, 084904.

Dovstam, K. (2000). Augmented Hooke's law based on alternative stress relaxation models. *Computational Mechanics, 26*, 90–103.

Gibson, L. J., & Ashby, M. F. (1997). *Cellular solids – Structure and properties* (2nd ed.). Cambridge: Cambridge University Press [p. 510].

Göransson, P., & Hörlin, N. E. (2010). Vibro-acoustics modelling of anisotropic porous elastic materials. A preliminary study of the influence of anisotropy on the predicted performance in a multi-layer arrangement. *Acta Acustica United with Acustica, 96*, 258–265.

Guastavino, R., & Göransson, P. (2007). A 3D displacement measurement methodology for anisotropic porous cellular foam materials. *Polymer Testing, 26*, 11–719.

Hörlin, N. E., & Göransson, P. (2000). A 3-D hierarchical FE formulation of Biot's equations for elasto-acoustic modelling of porous media. *Journal of Sound and Vibration, 245*, 633–652.

Hörlin, N. E., & Göransson, P. (2010). Weak, anisotropic symmetric formulations of Biot's equations for vibro-acoustic modelling of porous elastic materials. *International Journal for Numerical Methods in Engineering, 82*, 1519–1540.

Jaouen, L., Renault, A., & Deverge, M. (2008). Elastic and damping characterizations of acoustical porous materials: Available experimental methods and applications to a melamine foam. *Applied Acoustics, 69*, 1129–1140.

Jones, R. M. (1999). *Mechanics of composite materials*. Philadelphia: Taylor and Francis [p. 519].

Lind Nordgren, E., Göransson, P., Deü, J.-F., & Dazel, O. (2013). Vibroacoustic response sensitivity due to relative alignment of two anisotropic poro-elastic layers. *Journal of the Acoustical Society of America, 133*, EL426–EL430.

Melon, M., Mariez, E., Ayrault, C., & Sahraoui, S. (1998). Acoustic and mechanical characterization of anisotropic open-cell foams. *Journal of the Acoustical Society of America, 104*, 2622–2627.

Průša, Vít, Rajagopal, K. R., & Saravanan, U. (2013). Fidelity of the estimation of the deformation gradient from data deduced from the motion of markers placed on a body that is subject to an inhomogeneous deformation field. *Journal of Biomechanical Engineering, 135*(8), 081004.

Rice, H. J., & Göransson, P. (1999). A dynamical model of light fibrous materials. *International Journal of Mechanical Sciences, 41*, 561–579.

Slawinski, M. A. (2010). *Waves and rays in elastic continua* (2nd ed.). World Scientific Publishing Company [p. 616].

Svanberg, K. (2002). A class of globally convergent optimization methods based on conservative convex separable approximations. *SIAM Journal of optimization, 12*, 555–573.